IEEE Photonics Journal
An IEEE Photonics Society Publication

Quasi-Parametric Chirped-Pulse Amplification Simultaneously Enables High Peak Power and High Average Power

Volume 11, Number 4, August 2019

Zhe Yin
Jingui Ma
Jing Wang
Peng Yuan
Guoqiang Xie
Liejia Qian

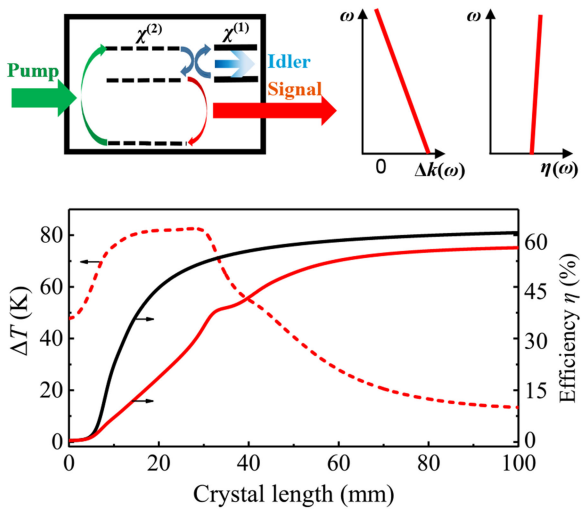

DOI: 10.1109/JPHOT.2019.2929175
1943-0655 © 2019 CCBY

Quasi-Parametric Chirped-Pulse Amplification Simultaneously Enables High Peak Power and High Average Power

Zhe Yin,[1] **Jingui Ma**,[1] **Jing Wang**,[1] **Peng Yuan**,[1] **Guoqiang Xie**,[1] **and Liejia Qian** [1,2]

[1]Key Laboratory for Laser Plasmas (Ministry of Education), Collaborative Innovation Center of IFSA (CICIFSA), School of Physics and Astronomy, Shanghai Jiao Tong University, Shanghai 200240, China
[2]Tsung-Dao Lee Institute, Shanghai Jiao Tong University, Shanghai 200240, China

DOI:10.1109/JPHOT.2019.2929175

Manuscript received April 4, 2019; revised July 6, 2019; accepted July 11, 2019. Date of publication July 17, 2019; date of current version August 1, 2019. This work was supported by the National Natural Science Foundation of China under Grant 61705128, Grant 61727820, and Grant 91850203; in part by the Science and Technology Commission of Shanghai Municipality under Grant 17YF1409100 and Grant 17ZR1414000. Corresponding author: Jingui Ma (email: majg@sjtu.edu.cn.)

Abstract: Ultrafast lasers with both high peak-power and high average-power will open new avenues for many applications. While conventional technologies of Ti:sapphire laser amplification and optical parametric amplification can achieve several tens of watts of average-power, scaling to a higher average-power is challenging due to thermal limitations. Here, we demonstrate that the quasi-parametric chirped-pulse amplification (QPCPA) can break this average-power barrier. QPCPA is proven robust against the thermal dephasing by obstructing the back-conversion effect. Numerical simulations show that QPCPA based on a Sm:YCOB crystal can support peak powers of 3 TW at 5 kHz and 13.5 PW at 1 Hz, with average powers exceeding 150 W in both cases. We also discuss the prospects of QPCPA with the recently proposed configuration of temperature-insensitive phase matching, which is promising to simultaneously achieve higher peak-power and higher average-power.

Index Terms: Quasi-parametric chirped-pulse amplification, thermal dephasing, high average power.

1. Introduction

Advances in intense lasers have opened a door to strong-field physics experiments, such as high harmonic generation (HHG) and laser-based particle acceleration [1]–[3]. Since strong-field phenomena are dependent on the intensity of the drive laser, increases in laser peak power have been a major concern over the past decades. Recently, laser peak power has been boosted greatly to multipetawatt levels by either laser-amplifier-based chirped-pulse amplification (CPA) or optical parametric chirped-pulse amplification (OPCPA) [4]–[7]. Such intense lasers generate an extreme intensity of $>10^{21}$ W/cm^2, which can promote laser-matter interactions into the relativistic regime [8]. However, contemporary intense lasers with a low repetition rate (10 Hz or less) are only suitable for exploring new phenomena. To promote applications of strong-field phenomena, the drive laser should have a sufficiently high repetition rate. A high-repetition-rate drive laser can increase the photon flux of HHG and may help to increase the signal-to-noise ratio of subsequent measurements and applications [9]. Future laser accelerators will require a kHz repetition rate to

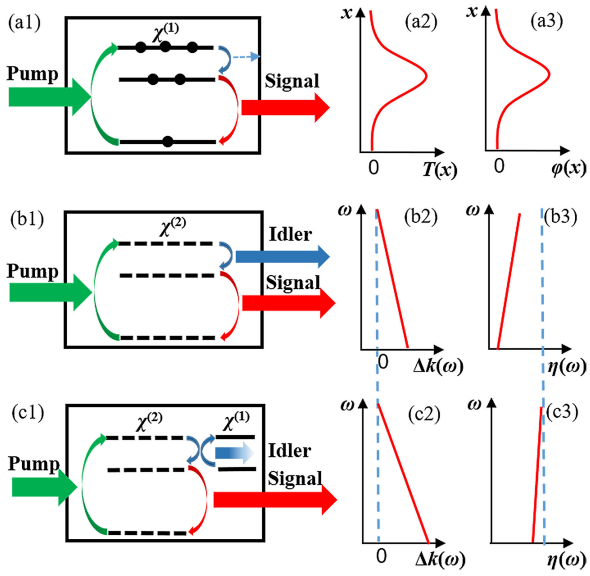

Fig. 1. Schematic diagrams and thermal effects of [(a1)∼(a3)] the laser amplifier, [(b1)∼(b3)] OPCPA, and [(c1)∼(c3)] QPCPA. (a1) A high-frequency pump wave amplifies a low-frequency signal wave through population inversion and stimulated emission. A nonradiative jump process is involved in the laser amplifier, which causes the thermal effect. (b1) In OPCPA, a high-frequency pump wave amplifies a low-frequency signal wave and simultaneously generates a low-frequency idler wave through the quadratic nonlinear polarization. (c1) QPCPA is similar to OPCPA, but the generated idler wave is absorbed by the nonlinear crystal. T(x) and φ(x) in (a2) and (a3) refer to the radial temperature gradient and the thermal lensing effect, respectively. $\Delta k(\omega)$ in (b2) and (c2) refers to thermal dephasing, and its influences on the conversion efficiency $\eta(\omega)$ are shown in (b3) and (c3).

produce high electron flux [10]. In addition, a high laser repetition rate is also favorable to avoid the space-charge effect in applications such as photoelectron spectroscopy [11]. Drive lasers with a both high peak power (>100 TW) and a high repetition rate (>100 Hz) are becoming increasingly attractive for strong-field physics [12]–[18].

High-repetition-rate operation of intense lasers is hampered by the thermal effect induced by gain medium absorption. The thermal effect is a result of the temperature-dependent refractive index and generally manifests itself as a thermal lensing effect in the spatial domain. For Ti:sapphire CPA lasers, the workhorse for driving strong-field physics, the Ti:sapphire crystal absorbs the pump light significantly and then dumps a portion of energy into the signal [Fig. 1(a1)]. The widely used configuration of end pumping and lateral cooling results in a radial temperature gradient across the crystal aperture [Fig. 1(a2)]. Such a radial temperature gradient will create a thermal lens [Fig. 1(a3)] owing to the thermal-induced radial change in the refractive index, which can distort the beam quality of the amplified signal [19]. Fortunately, the thermal lensing effect can be significantly suppressed by cryogenic cooling, because the thermal conductivity of the Ti:sapphire crystal increases and the dependence of the refractive index on temperature decreases with decreasing temperature [20]. With cryogenic cooling, a regenerative Ti:sapphire amplifier has produced an average power of 54 W at a repetition rate of 10 kHz [21].

Compared to Ti:sapphire systems, OPCPA can generate a higher average power since the nonlinear crystal does not involve pump absorption [Fig. 1(b1)]. The advance of thin-disk pump lasers with kilowatt-class average powers provides strong support for the development of such high-average-power OPCPA [12], [13]. The state-of-the-art OPCPA can deliver 88 W of average power [22]. Higher-average-power OPCPA still suffers from the thermal load due to the residual impurity absorption of the nonlinear crystal [23], [24]. As residual impurity absorption in OPCPA is much smaller than the pump absorption in Ti:sapphire lasers, the thermal lens in OPCPA is much weaker and can be neglected. On the other hand, the thermal dephasing effect in the frequency domain

may degrade the OPCPA efficiency [Figs. 1 (b2) and 1(b3)]. To achieve efficient conversion from the pump to the signal wave, the phase matching (PM) condition should be satisfied in OPCPA, i.e., $\Delta k = k_p - k_s - k_i = 0$, where k_p, k_s, and k_i are the wave vectors of the pump, signal, and idler waves, respectively. The required PM condition is usually realized with the aid of birefringence in nonlinear optical crystals, such as β-BBO [16]–[18], LBO [6], [25], and YCOB crystals [26], [27]. Heating of the crystal will change the refractive index and hence the PM condition [Fig. 1(b2)], which can degrade the conversion efficiency [Fig. 1(b3)] and the spatiotemporal quality of the output pulses. Such a thermal dephasing effect in OPCPA should be overcome to push the average power beyond 100 W.

Quasi-parametric chirped-pulse amplification (QPCPA) is a new scheme that enables efficient amplification of chirped signal pulses without back conversion by depleting the idler pulses [28]–[30], as schematically plotted in Fig. 1(c1). Intuitively, the depletion of the idler pulses removes the indispensable idler component for the back conversion process (i.e., signal+idler→pump). Inherently, idler absorption triggers a phase self-locking effect, which is the underlying mechanism for the suppression of back conversion [30]. The QPCPA scheme is characterized by a high signal efficiency, a broad bandwidth, and robustness against phase mismatching. The expected high signal efficiency and broad bandwidth can enhance its peak power scaling, while its robustness against phase mismatching allows a similar output stability to a conventional laser amplifier. The QPCPA scheme has been experimentally verified using a Sm:YCOB crystal [28]. This dedicated crystal is fabricated by doping rare-earth Sm^{3+} ions into the YCOB matrix, which leads to absorption in a broad spectral range around 1.5 μm (i.e., the idler spectrum). As mentioned above, the effect of thermal dephasing on signal amplification can be split into a two-step process: 1) the temperature rise induced by absorption results in a phase mismatch between the interacting waves, and 2) the phase mismatch degrades the signal amplification. It seems that artificial absorption of the idler wave may aggravate the thermal dephasing effect in QPCPA due to the increase in the temperature rise (i.e., aggravate the first step) [Fig. 1(c2)]. However, the inherent robust amplification against phase mismatching of QPCPA may partially counteract the thermal dephasing effect (i.e., suppress the second step) [Fig. 1(c3)]. Thus, QPCPA may still support high-repetition-rate and high-average-power operation, although it involves strong idler absorption. Therefore, it is necessary to illustrate the thermal dephasing effect and average power performance in QPCPA, which is the main subject of this theoretical study. QPCPA is proven to be a promising scheme for boosting intense lasers beyond average power of 100 W.

2. Numerical Model

In this manuscript, the thermal dephasing and average power performance of QPCPA is studied numerically. As there is little information about the thermal characteristics of the Sm:YCOB crystal, we adopt the data from the pure YCOB crystal by introducing idler absorption artificially. In fact, such an assumption is reasonable for a low doping concentration of Sm^{3+} (∼30%). Only the idler absorption (absorption coefficient ∼300/m) is taken into account, and the residual crystal absorptions of the signal (∼0.2/m) and pump (∼1/m) are neglected. By considering the effects of beam walk-off, diffraction and dispersion (up to third order) in QPCPA, the nonlinear coupled-wave equations under the slowly varying envelope approximation are given by

$$\frac{\partial A_p}{\partial z} + \rho_p \frac{\partial A_p}{\partial x} - \frac{i}{2k_p}\left(\frac{\partial^2 A_p}{\partial x^2} + \frac{\partial^2 A_p}{\partial y^2}\right) - \sum_{m=1}^{m=3} \frac{(-i)^{m-1}}{m!}\beta_{mp}\frac{\partial^m A_p}{\partial t^m} = -i\frac{\omega_p d_{eff}}{n_p c} A_s A_i e^{j\Delta k(T)z}, \tag{1}$$

$$\frac{\partial A_s}{\partial z} + \rho_s \frac{\partial A_s}{\partial x} - \frac{i}{2k_s}\left(\frac{\partial^2 A_s}{\partial x^2} + \frac{\partial^2 A_s}{\partial y^2}\right) - \sum_{m=1}^{m=3} \frac{(-i)^{m-1}}{m!}\beta_{ms}\frac{\partial^m A_s}{\partial t^m} = -i\frac{\omega_s d_{eff}}{n_s c} A_p A_i^* e^{-i\Delta k(T)z}, \tag{2}$$

$$\frac{\partial A_i}{\partial z} + \rho_i \frac{\partial A_i}{\partial x} - \frac{i}{2k_i}\left(\frac{\partial^2 A_i}{\partial x^2} + \frac{\partial^2 A_i}{\partial y^2}\right) - \sum_{m=1}^{m=3} \frac{(-i)^{m-1}}{m!}\beta_{mi}\frac{\partial^m A_i}{\partial t^m} = -i\frac{\omega_i d_{eff}}{n_i c} A_p A_s^* e^{-i\Delta k(T)z} - \frac{\alpha}{2}A_i, \tag{3}$$

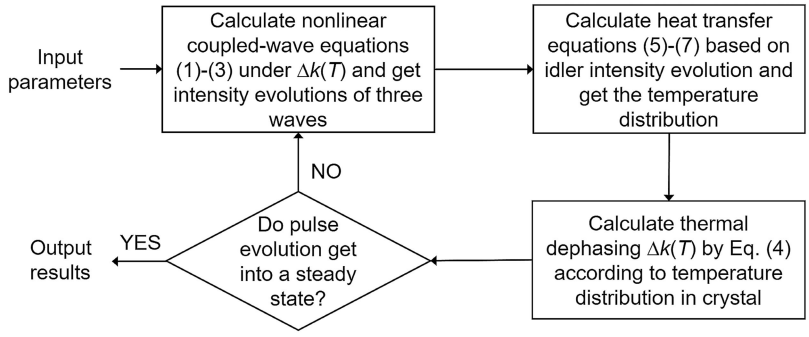

Fig. 2. Iterative algorithm for achieving a steady QPCPA.

where A_j, ω_j, and n_j, are the complex envelope, carrier frequency, and refractive index of wave j and $j = p, s$, and i refer to the pump (532 nm), signal (800 nm), and idler (1588 nm), respectively. c is the light speed in vacuum, $k_j = n_j w_j / c$ is the wavevector, and d_{eff} is the effective nonlinear coefficient. The mth-order dispersion coefficient of wave j, $\beta_{mj} = \partial^{(m)} k_j / \partial \omega^{(m)}$, represents the inverse of the group velocity, group-velocity dispersion, and third-order dispersion from $m = 1$ to 3, respectively. $\rho_p = 1.15^\circ$ is the walk-off angle of the pump wave in the x–z plane, and $\rho_s = 2.76^\circ$ ($\rho_i = 5.53^\circ$) corresponds to the intersection angle between k_s (k_i) and k_p for broadband noncollinear PM. Diffraction is considered in both transverse dimensions of x and y. $\alpha = 3\ \text{cm}^{-1}$ is the idler absorption coefficient. The temperature-dependent $\Delta k(T)$ represents thermal dephasing, which can be expanded into a Taylor series up to second order around a reference temperature T_0

$$\Delta k(T) = \Delta k(T_0) + \frac{\partial \Delta k}{\partial T}\Big|_{T=T_0} \Delta T + \frac{\partial^2 \Delta k}{\partial T^2}\Big|_{T=T_0} (\Delta T)^2, \tag{4}$$

where $\Delta T = T - T_0$ is the crystal temperature variation, and $T_0 = 293$ K is assumed in the following simulations.

The temperature distribution inside the crystal can be calculated from the heat transfer equation [31], [32],

$$\nabla^2 T = -\frac{Q}{\kappa} = \frac{\varepsilon_0 c \alpha n_i |A_i|^2}{2\kappa}, \tag{5}$$

where Q is heat source density caused by idler absorption, ε_0 is vacuum permittivity and κ is the thermal conductivity of Sm:YCOB, which is assumed to be 2 W/(m·K) in our simulation [33]. We adopt a lateral crystal cooling configuration, in which the temperature at the lateral face is fixed at T_0. At the two end surfaces, the convection boundary conditions are satisfied,

$$\kappa \frac{\partial T}{\partial z}\Big|_{z=0} = \mu (T_{z=0} - T_{air}), \tag{6}$$

$$-\kappa \frac{\partial T}{\partial z}\Big|_{z=L} = \mu (T_{z=L} - T_{air}), \tag{7}$$

where $\mu = 10$ W/(m^2·K) is the convection coefficient, and $T_{air} = 293$ K is the ambient temperature.

An iterative algorithm is performed by the MATLAB software to simulate a steady QPCPA [31], [32], as demonstrated in Fig. 2. At the beginning of this iterative algorithm, we assume a uniform crystal temperature of 293 K, and calculate the coupled-wave equations (1)–(3) to explore the intensity evolutions of three waves based on input parameters. Eqs. (1)–(3) were calculated by a symmetric split-step Fourier transform method with a step size of 50 μm. According to the absorption coefficient α and idler intensity evolution in crystal, we can get the heat source density Q in Eq. (5). Then, the heat transfer equation (5) is calculated by a finite difference method under the boundary conditions defined by Eqs. (6) and (7). In the finite difference method, the crystal

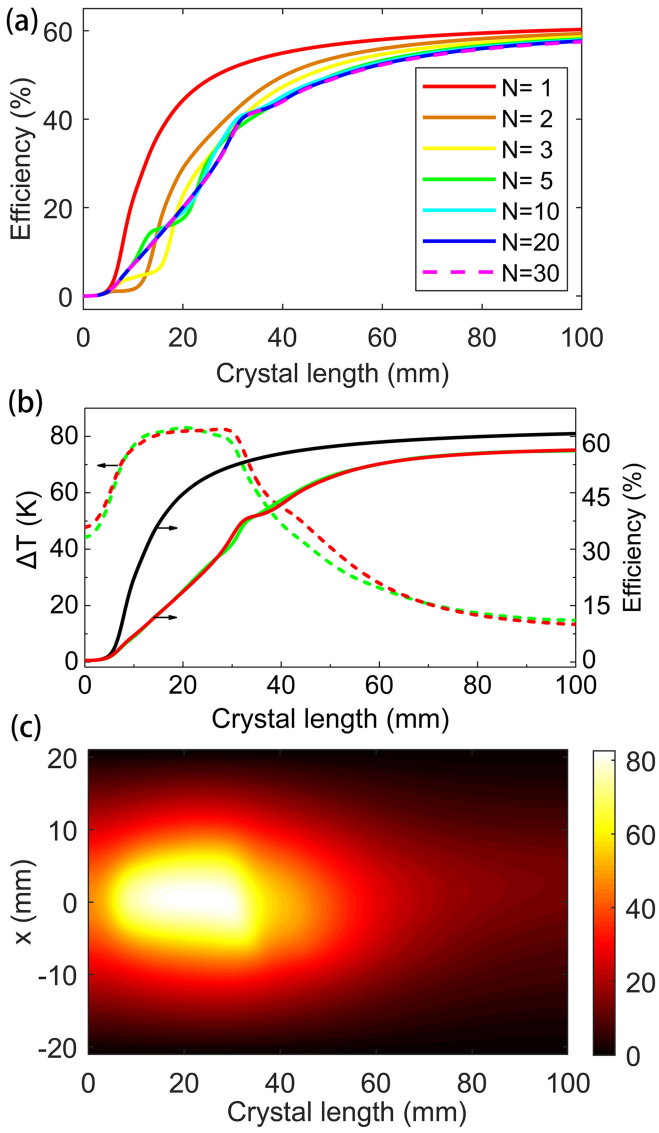

Fig. 3. (a) Intermediate calculation processes for signal efficiency with different numbers of Iterative cycle *N*. (b) Signal conversion efficiency (solid curve) and temperature rise (dashed curve) versus propagation distance in QPCPA. The black and red solid curves correspond to the conversion efficiencies without and with considering the thermal effect, respectively. The dashed curve presents the temperature rise in the transverse center (x = 0, y = 0) of the crystal. The green solid and dashed curves show the results with a cell size of 0.4 mm, while all the remaining results are obtained with a cell size of 0.7 mm. (c) Temperature rise distribution in the x-z plane. In the calculations, the average powers for the pump and seed signal are 100 W and 0.1 W, respectively. The pulse repetition rate is set to 1 kHz.

is discretized into many cubic cells with a size of 0.7 mm. The simulation results performed with such a cell size show no obvious difference with those obtained with a smaller cell size of 0.4 mm, as shown in Fig. 3(b). After finishing the calculation of Eqs. (5)–(7), the temperature distribution in crystal can be achieved, by which we can get the thermal dephasing $\Delta k(T)$ from Eq. (4). We then substitute this $\Delta k(T)$ into Eqs. (1)–(3) and recalculate the intensity distributions of three waves. Such an iteration continues until the temperature distribution and light intensities reach a steady state. Once the results converge, the iteration stops and outputs calculation results. To make the results converge well, it often needs at least 30 iteration cycles, which will cost about 20 hours on

a conventional desktop computer. In our simulations with a 40 $\times$ 40 $\times$ 100 mm Sm:YCOB crystal, a step size of 50 μm and a cell size of 0.7 mm were adopted by balancing the calculation precision and consuming time.

In addition to the thermal dephasing $\Delta k(T)$, the thermal expansion of the crystal may induce mechanical tensile stress and hence cause a crystal fracture [23]. To avoid the fracture problem, the highest crystal temperature should be controlled such that it is below the fracture temperature. Compared with the β-BBO crystal, which has a fracture temperature of 470 K [23], the YCOB crystal is more robust against thermal fractures because of its twice larger thermal conductivity and much weaker anisotropy in the thermal expansion coefficients [33]. The YCOB crystal has also been widely used in high-temperature piezoelectric sensing up to 1500 K [34]. Therefore, the Sm:YCOB crystal is expected to withstand a higher temperature rise ΔT than the β-BBO crystal. Nevertheless, we set the acceptable maximum ΔT to 300 K for estimating the average power ceiling in the following simulations.

3. Result and Discussion

3.1 Robust QPCPA Against Thermal Dephasing

First, a QPCPA process pumped with 532-nm pulses with a 1 kHz repetition rate and 100-W average power is simulated to calculate the thermal dephasing effect and its influence on signal amplification. Spatiotemporally, a Gaussian pump and chirped signal are assumed to have the same full-width-at-half-maximum (FWHM) duration of 10 ps and the same FWHM beam width of 10 mm. The pump and signal energies are 100 mJ and 0.1 mJ, respectively. The signal pulse at 800 nm has a FWHM bandwidth of 100 nm. QPCPA with a 40-mm-wide, 100-mm-long Sm:YCOB crystal is studied numerically. Obviously, such high-average-power QPCPA will suffer from thermal dephasing. Fig. 3(a) shows the iteration process for the signal efficiency. At the beginning of iteration, the result of signal efficiency changes with the number of iteration N. With the increase of N, such change becomes smaller. The calculation converges when $N > 20$. And the results at $N = 30$ are delivered for further analysis, as shown by the red solid curve in Fig. 3(b). For a comparison, a similar QPCPA process but without considering the thermal dephasing effect is also simulated, as shown by the black solid curve in Fig. 3(b).

Figs. 3(b) and 3(c) summarize the signal efficiency and evolution of the temperature rise within the crystal. In the artificially nonthermal situation, the signal efficiency always continues growing towards quantum-limited efficiency without suffering back conversion [black solid curve in Fig. 3(b)]. In a real situation with thermal dephasing, the signal efficiency degrades, especially in the first half of the crystal [red solid curve in Fig. 3(b)]. This degradation is attributed to thermal dephasing caused by idler absorption, as implied by Eq. (4). According to the red solid curve in Fig. 3(b), rapid growth in the signal efficiency occurs in the thickness range of $\sim$7 mm to $\sim$50 mm. In this thickness range, the idler wave is also generated sufficiently and is then absorbed strongly by the crystal, which leads to a significant temperature rise up to 80 K [Fig. 3(c) and the dashed curve in Fig. 3(b)]. This temperature rise is well below the acceptable maximum temperature rise of $\Delta T = 300$ K for crystal safety. In the second half of the crystal, QPCPA falls into the strong saturation regime. In this regime, the influence of thermal effect decreases significantly because of the slow generation of the idler wave. The signal efficiency keeps increasing and finally reaches $\sim$58% in the output end of crystal, indicating an amplified signal energy of 58 mJ. Assuming a typical compression throughput of 80% [17], the pulse energy after compression is approximately 46 mJ, corresponding to an average power of 46 W at a repetition rate of 1 kHz.

As shown in Fig. 3, QPCPA can still support highly efficient signal amplification in the high-average-power regime, manifesting the robustness of QPCPA against thermal dephasing. By a comparison with the ideal nonthermal situation, further simulations in Figs. 4 and 5 also illustrate that the thermal dephasing effect has little influence on the spatiotemporal qualities of the output signal. The nearly full pump depletion in both the temporal domain [Fig. 4(b)] and the spatial domain [Fig. 5(c)] proves the high conversion efficiency and the suppression of back conversion

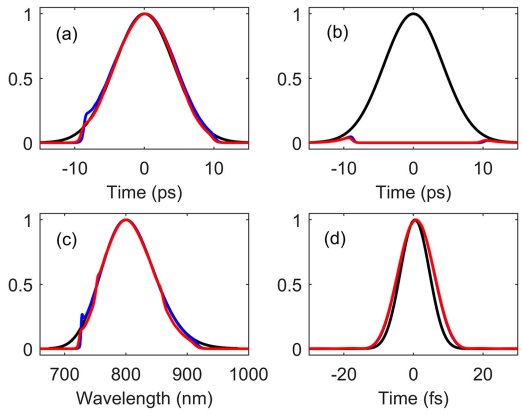

Fig. 4. Output pulses of the (a) chirped signal and (b) pump from QPCPA simulated in Fig. 3. (c) Signal spectrum and (d) its Fourier transform limit. The red (blue) curve refers to the situation with (without) considering the thermal effect, while the black curves indicate the incidence.

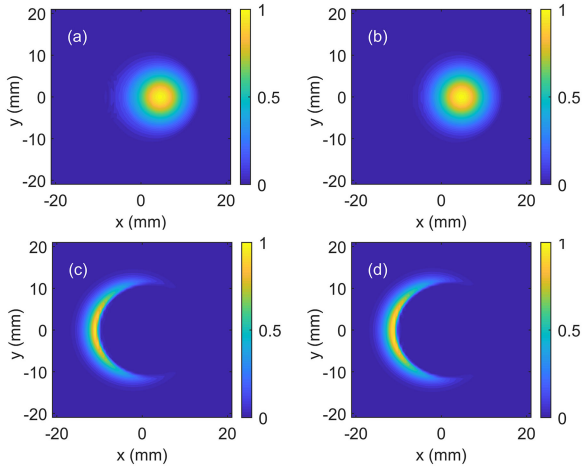

Fig. 5. Output beams of the (a) signal and (c) pump from QPCPA simulated in Fig. 3 when the thermal dephasing is considered. Output beams of the (b) signal and (d) pump when thermal dephasing is not considered.

by QPCPA. The crescent-shaped residual pump beam, in both the thermal situation [Fig. 5(c)] and the nonthermal situation [Fig. 5(d)], is induced by the walk-off between the pump and signal beams. There is also no obvious distortion of the signal beam [Figs. 5(a) and 5(b)]. The pulse profile and spectrum of the chirped signal before compression are consistent with those in the ideal nonthermal situation [Figs. 4(a) and 4(c)]. The similarity in the shapes of the pulse and the spectrum is a result of the mapping between the frequency and time of a chirped signal. After compression, the signal pulse duration recovers to ∼11 fs, close to its Fourier transform limit [Fig. 4(d)]. Considering the amplified signal energy of 46 mJ, the peak power of the compressed signal pulses reaches ∼4.2 TW. Both the average power and peak power of this QPCPA process are comparable to the reported state-of-the-art results (53 W, 5.5 TW) for OPCPA pumped by a much higher energy [17].

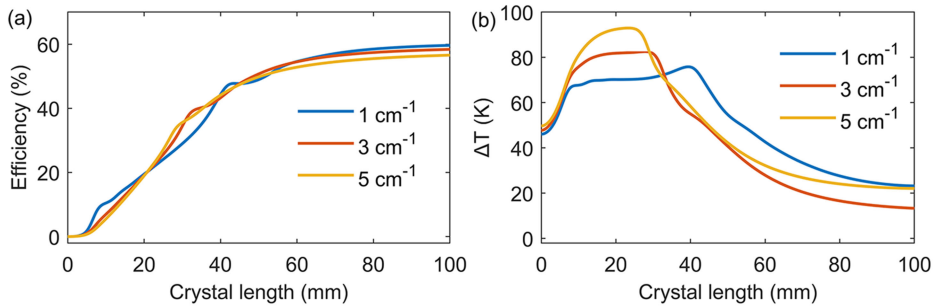

Fig. 6. (a) Calculated signal efficiency and (b) temperature rise in the transverse center of the crystal. The blue, red and orange curves correspond to the cases of $\alpha = 1$ cm^{-1}, 3 cm^{-1}, and 5 cm^{-1}, respectively. The adopted simulation parameters (except α) are the same as those in Fig. 3.

3.2 Influence of Idler Absorption

The idler absorption coefficient is a crucial parameter in QPCPA. Weak absorption might not deplete the idler sufficiently, while overly strong absorption may increase thermal dephasing and degrade the QPCPA performance. On the other hand, the idler absorption of Sm:YCOB is not uniform over the spectrum. Thus, it is necessary to study the amplification behavior of QPCPA as the absorption coefficient α is varied. In addition to the above adopted $\alpha = 3$ cm^{-1}, QPCPA processes with $\alpha = 1$ cm^{-1} and 5 cm^{-1} are also simulated in this paper. All the calculation results are plotted in Fig. 6. The significant variation in α has little effect on the signal efficiency of QPCPA, as shown in Fig. 6(a). In all three cases, a similar signal efficiency of $\sim$60% can be achieved. Although the absorption coefficient is altered five times from $\alpha = 1$ cm^{-1} to 5 cm^{-1}, the temperature rise ΔT inside the crystal does not vary much and increases by only 30% [Fig. 6(b)]. This result is reasonable because there is no simple linear dependence between ΔT and α in QPCPA, as implied by Eq. (5). Since the total absorbed idler energy will be limited by the fixed pump energy, ΔT should not vary too much with a change in α. A larger α leads to absorption of the idler energy over a shorter crystal length, so ΔT presents a higher peak value over a shorter distance. Owing to such a distribution of ΔT, the absorption coefficient affects the signal efficiency more obviously in the front of the crystal before 40 mm [Fig. 6(a)]. However, the amplification enters a long-distance saturation regime in the end of the crystal after 50 mm. Such a saturation behavior on efficiency is attributed to the obstruction of back conversion by QPCPA. The numerical study shows that QPCPA is robust against a variation in the idler absorption, which suggests that the nonuniform absorption spectrum of Sm:YCOB will not significantly affect the performance of QPCPA.

3.3 Scalability of the Average Power and Peak Power

The peak temperature rise ΔT of the crystal is below 100 K in the above simulations, so it is possible to further scale up the average power until $\Delta T = 300$ K. In the following simulations, we study QPCPA with the same parameters as those in section 3.1 (the pump energy is fixed at 100 mJ) but with a varied repetition rate (i.e., varied pump average power). To keep the temperature rise below the maximum acceptable value $\Delta T = 300$ K, the repetition rate can be increased to 5 kHz, as shown by the green curve in Fig. 7(b). At this repetition rate, the signal efficiency can still reach a quite high value of $\sim$52% [green curve in Fig. 7(a)], indicating an amplified signal energy of 52 mJ. After compression with a typical throughput of 80%, the 5 kHz, 41.6 mJ signal pulse corresponds to an average power of $\sim$200 W. Taking into account the compressed pulse duration of 13.6 fs at 5 kHz [green curve in the inset of Fig. 7(a)], the signal pulse will have a peak power of $\sim$3 TW. A further increase in the repetition rate or pump average power may be possible by decreasing the crystal cooling temperature. Although the efficiency evolutions present notable differences among the three cases with repetition rates of 1 kHz, 2 kHz, and 5 kHz, all of them show

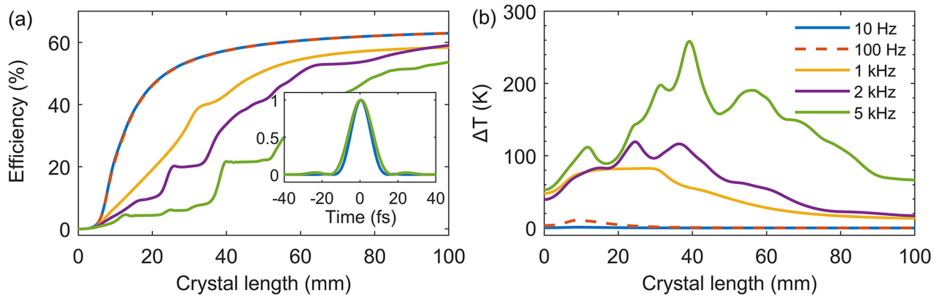

Fig. 7. (a) Calculated signal efficiency and (b) temperature rise in the transverse center of the crystal. The adopted simulation parameters (except the repetition rate) are the same as those in Fig. 3. The blue, red-dashed, yellow, purple and green curves represent the simulations at repetition rates of 10 Hz, 100 Hz, 1 kHz, 2 kHz and 5 kHz, respectively. The inset in (a) shows the Fourier-transform-limited compressed pulses at 10 Hz and 5 kHz, respectively.

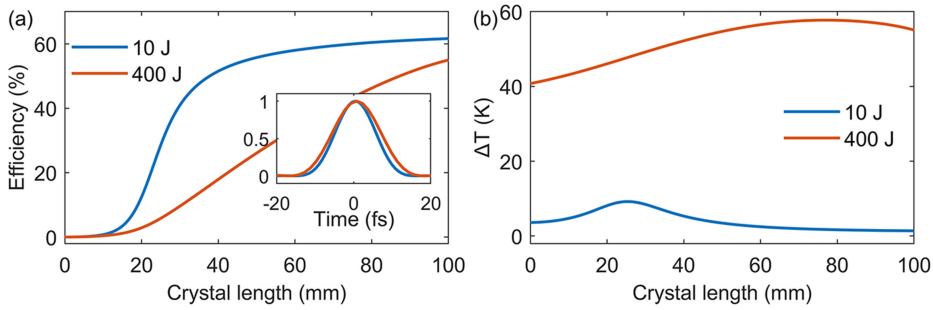

Fig. 8. (a) Calculated signal efficiency and (b) temperature rise in the transverse center of the crystal. The pump and seed signal intensities are 2.5 GW/cm^2 and 2.5 MW/cm^2, respectively. The repetition rate is fixed at 1 Hz. The blue, and red curves represent the simulations at pump energies of 10 J and 400 J, respectively. The inset in (a) shows the Fourier-transform-limited compressed pulses when the pump energy is 10 J and 400 J, respectively.

saturation characteristic to some extent when the crystal length exceeds 60 mm. Higher repetition rate will result in higher temperature rise and thus a severer thermal dephasing, which causes the degradation of gain coefficient and leads to the difference in efficiency evolution. Nevertheless, QPCPA is robust against thermal dephasing, so all the signal efficiencies keep growing with the increase of crystal length. Fig. 7 also gives the signal efficiency at much lower repetition rates of 10 Hz or 100 Hz, which corresponds to the nonthermal situation [black curve in Fig. 3(b)]. Obviously, the thermal dephasing effect can be neglected at repetition rates of $\leq$100 Hz in our simulations.

In the above simulations, the high-average-power performance of QPCPA was considered. For strong-field physics applications, higher-peak-power QPCPA will be of interest. To this end, we lower the repetition rate to 1 Hz and evaluate the peak power scalability of QPCPA. A large-aperture (120 mm) Sm:YCOB crystal is used in the simulations [35]. The pump pulse and chirped signal pulse are assumed to have the same Gaussian pulse profile with a duration of 2 ns and a same flat-top beam profile. The beam widths are adjusted at different pump energies to fix the pump intensity at 2.5 GW/cm^2 and the seed signal intensity at 2.5 MW/cm^2. At a pump energy of 10 J, QPCPA can fall into the high saturation regime, and the signal efficiency approaches the quantum limit [blue curve in Fig. 8(a)]. The signal pulse with an energy of 6.2 J, if compressed to 12 fs as shown by the blue curve in the inset of Fig. 8(a) with a throughput of 80%, has a peak power of 0.4 PW. In this case, the crystal temperature rise of $<$10 K [blue curve in Fig. 8(b)] can be neglected. By further increasing the pump energy to 400 J, the signal efficiency, although increases slowly, can still reach $\sim$55% [red curve in Fig. 8(a)]. After compression with a throughput of 80%,

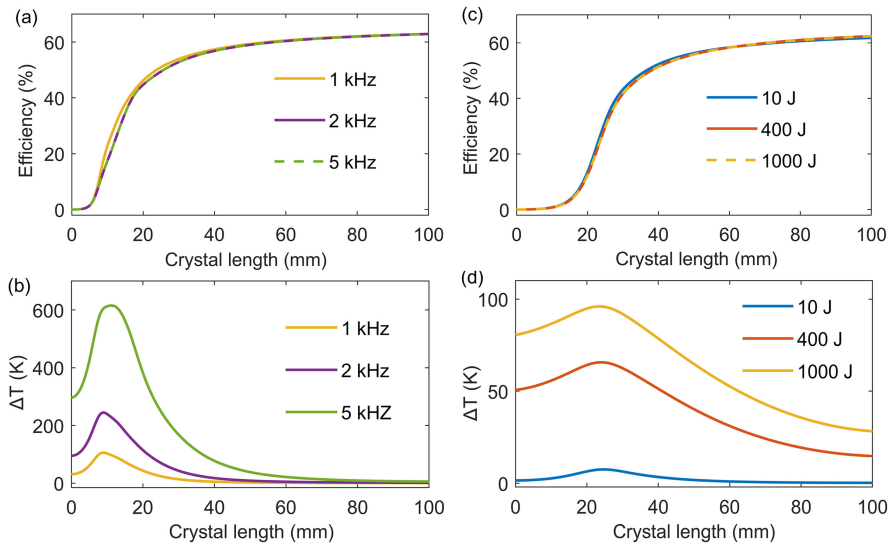

Fig. 9. (a) Signal efficiency and (b) temperature rise for the same QPCPA process as that of Fig. 7 but with $\partial\Delta k/\partial T = 0$. (c) Signal efficiency and (d) temperature rise for the same QPCPA process as that of Fig. 8 but with $\partial\Delta k/\partial T = 0$. In (c) and (d), the beam widths are adjusted to 16 mm, 100 mm, and 160 mm for the 10 J, 400 J, and 1000 J pump cases, respectively, to fix the pump intensity at 2.5 GW/cm^2. The crystal apertures are set to 25 mm, 150 mm, and 245 mm, with each of which being equal to approximately 1.5 times the corresponding beam width.

the signal pulse has an energy of ~176 J and a pulse duration of 13 fs [red curve in the inset of Fig. 8(a)], corresponding to a peak power of 13.5 PW. The crystal temperature rise in the 1-Hz, 13.5-PW QPCPA process is only 60 K [red curve in Fig. 8(b)], which is still far from the maximum acceptable temperature rise of $\Delta T = 300$ K, although the average power is as high as approximately 176 W. In large-aperture QPCPA systems, therefore, the thermal dephasing effect is no longer the major factor limiting the peak-power scaling at low repetition rates. In single-shot mode, the thermal effect definitely has no influence on the signal conversion efficiency owing to a large time interval between two successive shots.

3.4 QPCPA With Temperature-Insensitive Noncollinear PM

According to Eq. (4), thermal dephasing mainly arises from the phase-mismatch term $\partial\Delta k/\partial T$. It is obvious that the thermal dephasing effect in QPCPA can be significantly suppressed if enabling $\partial\Delta k/\partial T = 0$. Previously, temperature-insensitive second harmonic generation was achieved by selecting a specific nonlinear crystal with $\partial\Delta k/\partial T = 0$ [36]. However, this will not be possible for QPCPA with a dedicated crystal having strong idler absorption. In the previous section of this paper, we studied QPCPA with broadband noncollinear PM ($\partial\Delta k/\partial\lambda = 0$, but $\partial\Delta k/\partial T \neq 0$). On the other hand, the noncollinear angle ρ_s between the signal and pump can be utilized for temperature-insensitive PM ($\partial\Delta k/\partial T = 0$, but $\partial\Delta k/\partial\lambda \neq 0$). Such a temperature-insensitive nonlinear PM configuration has been applied to OPCPA, resulting in a five-fold enhancement in the temperature acceptance [37]. In the QPCPA process with a 532-nm pump and an 800-nm seed, either $\partial\Delta k/\partial T = 0$ or $\partial\Delta k/\partial\lambda = 0$ can be achieved by setting the noncollinear PM angle to $\rho_s = 6.12^\circ$ or $\rho_s = 2.68^\circ$ in the XY plane of the Sm:YCOB crystal, respectively. As these two noncollinear angles are not equal, angular dispersion of the seed signal must be introduced to ensure broadband PM if we set ρ_s to 6.12° for $\partial\Delta k/\partial T = 0$, as in [37]. The required angular dispersion for the signal is approximately 104 μrad/nm, which can be produced or compensated by slightly misaligning the pulse stretcher or compressor.

For comparison purposes, here we study QPCPA with both $\partial\Delta k/\partial T = 0$ and $\partial\Delta k/\partial\lambda = 0$ and summarize the results in Fig. 9. Because the PM is no longer sensitive to the crystal temperature

rise, the signal efficiencies in Figs. 9(a) and 9(c) nearly overlap with those in the ideal nonthermal case. Thus, the thermal dephasing effect is significantly suppressed in QPCPA with temperature-insensitive PM. The high signal efficiency also facilitates idler generation; thus, the crystal temperature rise at a high repetition rate shown in Fig. 9(b) is higher than the corresponding case in Fig. 7. On the other hand, the temperature rise at a low repetition rate shown in Fig. 9(d) has no obvious difference with respect to the corresponding case in Fig. 8. When the pump energy is increased to 1000 J, the temperature rise at a 1 Hz repetition rate is still below 100 K. It is expected that both temperature- and wavelength-insensitive QPCPA can support a peak power up to 100 PW at 1 Hz without suffering from significant thermal dephasing.

4. Summary

In this manuscript, we focus on enhancing the average power of intense laser by tackling the thermal dephasing effect encountered in parametric amplifiers. We demonstrate a thermal-dephasing-insensitive QPCPA scheme with the potential to overcome the 100-W average power barrier of current intense lasers. As the average power of a laser confines the product of its peak power and repetition rate, the enhancement of average power by QPCPA not only increases the repetition rate of a high peak-power laser, but also increases the peak power under a fixed repetition rate. By numerical simulations, we have demonstrated two examples of high-average-power QPCPA with different peak powers. The first example is a 200-W QPCPA with a moderate peak power of 5 TW and a high repetition rate of 5 kHz, which is an ideal drive source for high harmonic generation and photoelectron spectroscopy [9], [11]. The second example is a 176-W QPCPA with a high peak power of 13.5 PW and a repetition rate of 1 Hz, which can be applied in laser plasma acceleration and laboratory astrophysics [10]. We finally discuss the suppression of thermal dephasing by implementing the QPCPA in a temperature-insensitive phase matching configuration, and show the prospect of constructing a 1 Hz, 100 PW laser by QPCPA. This thermal-dephasing-suppressed QPCPA scheme can not only be used in strong-field physics applications, but also be applied to ultrafast nonlinear optics, high-speed optical communications and other frontiers demanding high average power [38]–[40]. Future improvement of the average power of QPCPA depends on the depletion of idler pulses by some non-absorption methods.

References

[1] T. Popmintchev *et al.*, "Bright coherent ultrahigh harmonics in the keV X-ray regime from mid-IR femtosecond lasers," *Science*, vol. 336, no. 6086, pp. 1287–1291, 2012.
[2] J. Breuer and P. Hommelhoff, "Laser-based acceleration of nonrelativistic electrons at a dielectric structure," *Physical Rev. Lett.*, vol. 111, no. 13, 2013, Art. no. 134803.
[3] J. Weisshaupt *et al.*, "High-brightness table-top hard X-ray source driven by sub-100-femtoseocnd mid-infrared pulses," *Nature Photon.*, vol. 8, no. 12, pp. 927–930, 2014.
[4] Z. Wang, C. Liu, Z. Shen, Q. Zhang, H. Teng, and Z. Wei, "High-contrast, 1.16 PW Ti:sapphire laser stystem combined with a doubled chirped-pulse amplification scheme and a femtosecond optical parametric amplifier," *Opt. Lett.*, vol. 36, no. 16, pp. 3194–3196, 2011.
[5] Y. Chu *et al.*, "High-energy large-aperture Ti:sapphire amplifier for 5 PW laser pulses," *Opt. Lett.*, vol. 40, no. 21, pp. 5011–5014, 2015.
[6] X. Zeng *et al.*, "Multi-petawatt laser facility fully based on optical parametric chirped-pulse amplification," *Opt. Lett.*, vol. 42, no. 10, pp. 2014–2017, 2017.
[7] C. Danson, D. Hillier, N. Hopps, and D. Neely, "Petawatt class lasers worldwide," *High Power Laser Sci. Eng.*, vol. 3, 2015, Art. no. e3.
[8] G. A. Mourou, T. Tajima, and S. V. Bulanov, "Optics in the relativistic regime," *Rev. Modern Phys.*, vol. 78, no. 2, pp. 309–371, 2006.
[9] S. Hädrich *et al.*, "High photon flux table-top coherent extreme-ultraviolet sourve," *Nature Photon.*, vol. 8, no. 10, pp. 779–783, 2014.
[10] G. Mourou, B. Brocklesby, T. Tajima, and J. Limpert, "The future is fibre accelerators," *Nature Photon.*, vol. 7, no. 4, pp. 258–261, 2013.
[11] S. Passlack, S. Mathias, O. Andreyev, D. Mittnacht, M. Aeschlimann, and M. Bauer, "Space charge effects in photoemission with a low repetition, high intensity femtosecond laser source," *J. Appl. Phys.*, vol. 100, no. 2, 2006, Art. no. 024912.
[12] H. Fattahi *et al.*, "Third-generation femtosecond technology," *Optica*, vol. 1, no. 1, pp. 45–63, 2014.

[13] B. A. Reagan *et al.*, "Scaling diode-pumped, high energy picosecond lasers to kilowatt average power," *High Power Laser Sci. Eng.*, vol. 6, 2018, Art. no. e11.
[14] A. Vaupel, N. Bodnar, B. Webb, L. Shah, and M. Richardson, "Concepts, performance review, and prospects of table-top, few-cycle optical parametric chirped-pulse amplification," *Opt. Eng.*, vol. 53, no. 5, 2014, Art. no. 051507.
[15] R. Clady, Y. Azamoum, L. Charmasson, A. Ferré, O. Utéza, and M. Sentis, "22 W average power multiterawatt femtosecond laser chain enabling 10^{19} W/cm^2 at 100 Hz," *Appl. Phys. B*, vol. 124, no. 5, 2018, Art. no. 89.
[16] J. Rothhardt, S. Demmler, S. Hädrich, J. Limpert, and A. Tünnermann, "Octave-spanning OPCPA system delivering CEP-stable few-cycle pulses and 22 W of average power at 1 MHz repetition rate," *Opt. Express*, vol. 20, no. 10, pp. 10870–10878, 2012.
[17] R. Budriūnas *et al.*, "53 W average power CEP-stabilized OPCPA system delivering 5.5 TW few cycle pulses at 1 kHz repetition rate," *Opt. Express*, vol. 25, no. 5, pp. 5797–5806, 2017.
[18] S. Prinz *et al.*, "Thin-disk pumped optical parametric chirped pulse amplifier delivering CEP-stable multi-mJ few-cycle pulses at 6 kHz," *Opt. Express*, vol. 26, no. 2, pp. 1108–1124, 2018.
[19] G. Wagner, M. Shiler, and V. Wulfmeyer, "Simulations of thermal lensing of a Ti:Sapphire crystal end-pumped with high average power," *Opt. Express*, vol. 13, no. 20, pp. 8045–8055, 2005.
[20] M. Zavelani-Rossi, F. Lindner, C. Le Blanc, G. Chériaux, and J. P. Chambaret, "Control of thermal effects for high intensity Ti:sapphire laser chains," *Appl. Phys. B*, vol. 70, no. 1, pp. S193–S196, 2000.
[21] I. Matsushima, H. Yashiro, and T. Tomie, "10 kHz 54 W Ti:sapphire regenerative amplifier as a pumping laser of a laser-plasma x-ray source," *Int. Soc. Opt. Photon.*, vol. 7022, 2008, Art. no. 70220M.
[22] K. Mecseki *et al.*, "High average power 88 W OPCPA system for high-repetition-rate experiments at the LCLS x-ray free-electron laser," *Opt. Lett.*, vol. 44, no. 5, pp. 1257–1260, 2019.
[23] J. Rothhardt, S. Demmler, S. Hädrich, T. Peschel, J. Limpert, and A. Tünnermann, "Thermal effects in high average power optical parametric amplifiers," *Opt. Lett.*, vol. 38, no. 5, pp. 763–765, 2013.
[24] R. Riedel *et al.*, "Thermal properties of borate crystals for high power optical parametric chirped-pulse amplification," *Opt. Express*, vol. 22, no. 15, pp. 17607–17619, 2014.
[25] L. Yu *et al.*, "Optimization for high-energy and high-efficiency broadband optical parametric chirped-pulse amplification in LBO near 800 nm," *Opt. Lett.*, vol. 40, no. 14, pp. 3412–3415, 2015.
[26] Z. M. Liao, I. Jovanovic, C. A. Ebbers, Y. Fei, and B. Chai, "Energy and average power scalable optical parametric chirped-pulse amplification in yttrium calcium oxyborate," *Opt. Lett.*, vol. 31, no. 9, pp. 1277–1279, 2006.
[27] L. Yu *et al.*, "Experimental demonstration of joule-level non-collinear optical parametric chirped-pulse amplification in yttrium calcium oxyborate," *Opt. Lett.*, vol. 37, no. 10, pp. 1712–1714, 2012.
[28] J. Ma *et al.*, "Quasi-parametric amplification of chirped pulses based on a Sm^{3+}-doped yttrium calcium oxyborate crystal," *Optica*, vol. 2, no. 11, pp. 1006–1009, 2015.
[29] J. Ma, J. Wang, P. Yuan, G. Xie, and L. Qian, "Origin and suppression of back conversion in a phase-matched nonlinear frequency down-conversion process," *Chin. Opt. Lett.*, vol. 15, no. 2, pp. 59–62, 2017.
[30] J. Ma *et al.*, "Broadband, efficient, and robust quasi-parametric chirped-pulse amplification," *Opt. Express*, vol. 25, no. 21, pp. 25149–25164, 2017.
[31] S. Seidel and G. Mann, "Numerical modeling of thermal effects in nonlinear crystals for high-average-power second harmonic generation," *Int. Soc. Opt. Photon.*, vol. 2989, pp. 204–215, 1997.
[32] M. Sabaeian, L. Mousave, and H. Nadgaran, "Investigation of thermally-induced phase mismatching in continous-wave second harmonic generation: A theoretical model," *Opt. Express*, vol. 18, no. 18, pp. 18732–18743, 2010.
[33] D. N. Nikogosyan, *Nonlinear Optical Crystals: A Complete Survey*. Berlin, Germany: Springer, 2005.
[34] X. Jiang, K. Kim, S. Zhang, J. Johnson, and G. Salazar, "High-temperature piezoelectric sensing," *Sensor*, vol. 14, no. 1, pp. 144–169, 2014.
[35] X. Tu, S. Wang, K. Xiong, Y. Zheng, and E. Shi, "Research on growth and defects of 5 in. YCOB single crystal," *J. Crystal Growth*, vol. 488, pp. 23–28, 2018.
[36] C. E. Barker, D. Eimerl, and S. P. Velsko, "Temperature-insensitive phase matching for second-harmonic generation in deuterated l-arginine phosphate," *J. Opt. Soc. Amer. B*, vol. 8, no. 12, pp. 2481–2492, 1991.
[37] D. Tang *et al.*, "Temperature- and wavelength-insensitive parametric amplification enabled by noncollinear achromatic phase matching," *Scientific Rep.*, vol. 6, 2016, Art. no. 36059.
[38] S. Barua, N. Das, S. Nordholm, and M. Razaghi, "Comparison of pulse propagation and gain saturation characteristics among different input pulse shapes in semiconductor optical amplifiers," *Opt. Commun.*, vol. 359, pp. 73–78, 2016.
[39] N. K. Das, T. Kawazoe, Y. Yamayoshi, and H. Kawaguchi, "Analysis of optical phase-conjugate characteristics of picosecond four-wave mixing in semiconductor optical amplifiers," *IEEE J. Quantum Electron.*, vol. 37, no. 1, pp. 55–62, Jan. 2001.
[40] M. Premaratne, D. Nešić, and G. P. Agrawal, "Pulse amplification and gain recovery in semiconductor optical amplifiers: A systematic analytical approach," *J. Lightw. Technol.*, vol. 26, no. 12, pp. 1653–1660, Jun. 2008.